INTERNATIONAL JOURNAL FOR NUMERICAL METHODS IN FLUIDS
Int. J. Numer. Meth. Fluids 2003; **41**:1119–1135 (DOI: 10.1002/fld.486)

Large-eddy simulation with complex 2-D geometries using a parallel finite-element/spectral algorithm

D. O. Snyder[1,*] and G. Degrez[2,†]

[1] *Mechanical & Aerospace Engineering Department, Utah State University, U.S.A.*
[2] *von Karman Institute for Fluid Dynamics, Belgium*

SUMMARY

A parallel stabilized finite-element/spectral formulation is presented for incompressible large-eddy simulation with complex 2-D geometries. A unique discretization scheme is developed consisting of a streamline-upwind Petrov–Galerkin/Pressure-Stabilized Petrov–Galerkin (SUPG/PSPG) finite-element discretization in the 2-D plane with a collocated spectral/pseudospectral discretization in the out-of-plane direction. This formulation provides an efficient approach for solving 3-D flows over arbitrary 2-D geometries. Utilizing this discretization and through explicit temporal treatment of the non-linear terms, the system of equations for each Fourier mode is decoupled within each time step. A novel parallelization approach is then taken, where the computational work is partitioned in Fourier space. A validation of the algorithm is presented via comparison of results for flow past a circular cylinder with published values for $Re = 195$, 300, and 3900. Copyright © 2003 John Wiley & Sons, Ltd.

KEY WORDS: LES; finite-element methods; spectral methods; unstructured meshes; parallel

1. INTRODUCTION

Simulations of turbulent flows are difficult because of the large range of scales involved: the largest scales are on the order of the domain dimensions, while the smallest are on the order of the Kolmogorov length scale. Three basic approaches exist for handling turbulence using the Navier Stokes equations. The direct numerical simulation (DNS) approach involves directly solving the Navier Stokes equations with no modelling. Unfortunately, due to high computational cost, DNS is currently limited to very low Reynolds numbers and simple domain geometries. In the Reynolds-averaged Navier–Stokes (RANS) approach, all turbulent fluctuations are averaged out of the Navier Stokes equations and are replaced with a turbulence model. RANS solutions tend to suffer lack of accuracy and generality, both of which

* Correspondence to: D. O. Snyder, Sverdrup Technology Inc./TEAS Group, P.O. Box 1935, Eglin AFB, FL 32542, U.S.A.
† E-mail: degrez@vki.ac.be

Contract/grant sponsor: US Air Force Fellowship and NSF Graduate Research Fellowship
Contract/grant sponsor: US Office of Naval Research; contract/grant number: N00014-99-1-0834

Received 26 January 2002
Revised 22 November 2002

are attributed to the shortcomings of the turbulence models. The large-eddy simulation (LES) approach lies between the extremes of DNS and RANS—the large-scale motions are explicitly calculated, while small-scale motions are filtered out of the governing equations and modelled. This approach is better-suited than DNS for practical applications, and remedies some of the accuracy and generality issues of the RANS equations.

Because the large turbulent scales must be computed, LES calculations are inherently 3-D; 2-D LES does not exist in the same respect as 2-D RANS. However, computational simplifications can be made if the boundary geometry is 2-D and the flow is assumed periodic in the out-of-plane direction. With these assumptions, a finite-element (FE) discretization is appropriate for the in-plane discretization, while a spectral discretization is well-suited in the out-of-plane direction. The algorithm developed in this work utilizes this combined FE/spectral discretization, which results in several benefits, the most profound of which are listed below.

- Complex 2-D geometries can easily be accommodated using an unstructured triangle mesh.
- Storage requirements are reduced because only a single 2-D mesh (and its associated overhead) need be stored.
- Taking inspiration from Henderson [1], through careful treatment of the non-linear terms, the Fourier modes can be decoupled within each time step and the problem converted to solving a number of independent 2-D problems at each time step. This situation is less expensive than solving the 3-D problem, and also lends itself nicely to a parallel implementation.

The purpose of this paper is to present the FE/spectral LES algorithm that has been developed. In the 2-D plane, a streamline-upwind Petrov–Galerkin/pressure-stabilized Petrov–Galerkin (SUPG/PSPG) FE method [2] is employed using linear triangle elements. In the out-of-plane direction, a collocated spectral approach is used, with pseudospectral treatment [3] of the non-linear terms. Temporally, the discretization uses a combination of implicit and explicit second-order methods. Because it arises naturally from the discretization scheme, a unique parallelization approach is employed, where partitioning of the work is carried out in Fourier space.

Flow past a circular cylinder is adopted as an example test-case. The flowfield is rather interesting for use in numerical simulations because it contains several distinct flow characteristics including boundary layers, flow separation, shear layers, and a wake region. This case has been extensively studied both experimentally [4–6] and numerically [7–9], consequently a large amount of data is available for comparison.

2. GOVERNING EQUATIONS

Consider incompressible flow of a viscous fluid in the computational domain Ω with boundary $\Gamma = \Gamma_d \cup \Gamma_n$, where Γ_d is the portion of the boundary subject to Dirichlet boundary conditions and Γ_n is the portion subject to Neumann conditions. Adopting the LES approach, the governing equations are derived by applying a filtering operation to the constant-density Navier–Stokes equations. Utilizing the skew-symmetric form of the convective terms in order to

ensure conservation of kinetic energy and reduce aliasing errors [10], the resulting equations are

$$\frac{\partial \bar{u}_i}{\partial t} + \bar{u}_j \frac{\partial \bar{u}_i}{\partial x_j} + \frac{1}{2}\bar{u}_i \frac{\partial \bar{u}_j}{\partial x_j} = -\frac{\partial \bar{p}}{\partial x_i} + \nu \frac{\partial^2 \bar{u}_i}{\partial x_j \partial x_j} + \frac{\partial \tau_{ij}}{\partial x_j} \quad \text{in } \Omega \tag{1}$$

$$\frac{\partial \bar{u}_i}{\partial x_i} = 0 \quad \text{in } \Omega \tag{2}$$

where the overbar denotes the filtering operation. In the above expressions, then, $\bar{u}_i$ is the filtered velocity, $\bar{p}$ is the filtered kinematic pressure (pressure divided by density), ν is the kinematic viscosity, and

$$\tau_{ij} = \overline{u_i u_j} - \bar{u}_i \bar{u}_j \tag{3}$$

This term, which accounts for the effects of the unresolved scales, is termed the subgrid-scale (SGS) Reynolds stress, and must be modelled.

Although it is an area of intense research, this work does not attempt to further the technology of SGS models. Instead, the focus is the development and implementation of the FE/spectral algorithm. Consequently, the common Smagorinski model with wall damping is implemented. Inclusion of more complicated models is a logical next step once the numerical algorithm has been developed. The Smagorinski model, originally proposed in 1963 [11], has provided reasonable results in countless studies. A Boussinesq approximation is first made, in which the SGS Reynolds stress is assumed proportional to the resolved strain:

$$\tau_{ij} = 2\nu_t \bar{S}_{ij} + \tfrac{1}{3}\tau_{\ell\ell}\delta_{ij} \tag{4}$$

where

$$\bar{S}_{ij} = \tfrac{1}{2}\left(\frac{\partial \bar{u}_i}{\partial x_j} + \frac{\partial \bar{u}_j}{\partial x_i}\right) \tag{5}$$

is the strain rate tensor of the filtered field, ν_t is the subgrid eddy viscosity, and δ_{ij} is the Kronecker delta. Substituting (4) into (1) and applying the incompressibility condition gives

$$\frac{\partial \bar{u}_i}{\partial t} + \bar{u}_j \frac{\partial \bar{u}_i}{\partial x_j} + \frac{1}{2}\bar{u}_i \frac{\partial \bar{u}_j}{\partial x_j} = -\frac{\partial \bar{P}}{\partial x_i} + (\nu + \nu_t)\frac{\partial^2 \bar{u}_i}{\partial x_j \partial x_j} + 2\frac{\partial \nu_t}{\partial x_j}\bar{S}_{ij} \quad \text{in } \Omega \tag{6}$$

where

$$\bar{P} = \bar{p} - \tfrac{1}{3}\tau_{\ell\ell} \tag{7}$$

From dimensional arguments, ν_t can be derived as

$$\nu_t = (f_w C_s)^2 \Delta^2 |\bar{S}| \tag{8}$$

where f_w is a wall-damping function, $C_s \approx 0.2$ is the so-called Smagorinski constant, Δ is the filter width

$$\Delta = V^{1/3} \tag{9}$$

with V being the element volume, and $|\bar{S}|$ is the local resolved strain rate

$$|\bar{S}| = (2\bar{S}_{ij}\bar{S}_{ij})^{1/2} \tag{10}$$

The filtering operation used in deriving (1) and (2) is assumed to be commutative with both temporal and spatial derivatives. The latter assumption is not valid near boundaries or when the filter width is non-uniform. This introduces errors into the SGS model, as characterized by Fureby and Tabor [12].

To obtain proper behaviour near the wall, damping of the eddy viscosity is introduced via f_w in (8). This is the so-called van Driest damping function [13] (originally developed for attached, non-separating flows) and is written

$$f_w = 1 - \exp\left(-\frac{\eta^+}{A^+}\right) \tag{11}$$

where $A^+ = 25$ and η^+ is the distance to the nearest wall in wall units,

$$\eta^+ = \frac{u_\tau \eta}{\nu} \tag{12}$$

with u_τ being the friction velocity, η the distance to the wall, and ν the kinematic viscosity.

Equations (1) and (2) are subject to Dirichlet and Neumann boundary conditions on Γ_d and Γ_n, respectively. Initial conditions $\bar{u}_i(x_i, t=0)$ are also given for the velocity field, pressure field, and boundary conditions.

3. NUMERICAL APPROACH

The governing equations are written in a form that separates the in-plane and out-of-plane components. Adopting the following notation:

$x_1,\ x_2$	in-plane co-ordinates
z	transverse co-ordinate
$\bar{u}_1,\ \bar{u}_2$	in-plane velocity components
$\bar{w}$	transverse velocity component
$p=(1,2),\ q=(1,2)$	in-plane coordinate indices

the governing equations (6) and (2) can be rewritten as

$$\begin{aligned}\frac{\partial \bar{u}_p}{\partial t} + \bar{u}_q \frac{\partial \bar{u}_p}{\partial x_q} + \bar{w}\frac{\partial \bar{u}_p}{\partial z} + \frac{1}{2}\bar{u}_p\left(\frac{\partial \bar{u}_q}{\partial x_q} + \frac{\partial \bar{w}}{\partial z}\right) \\ = -\frac{\partial \bar{P}}{\partial x_p} + (\nu + \nu_t)\left(\frac{\partial^2 \bar{u}_p}{\partial x_q \partial x_q} + \frac{\partial^2 \bar{u}_p}{\partial z^2}\right) + \frac{\partial \nu_t}{\partial x_q}\left(\frac{\partial \bar{u}_p}{\partial x_q} + \frac{\partial \bar{u}_q}{\partial x_p}\right) + \frac{\partial \nu_t}{\partial z}\left(\frac{\partial \bar{u}_p}{\partial z} + \frac{\partial \bar{w}}{\partial x_p}\right)\end{aligned} \tag{13}$$

$$\frac{\partial \bar{w}}{\partial t} + \bar{u}_q \frac{\partial \bar{w}}{\partial x_q} + \bar{w} \frac{\partial \bar{w}}{\partial z} + \frac{1}{2} \bar{w} \left(\frac{\partial \bar{u}_q}{\partial x_q} + \frac{\partial \bar{w}}{\partial z} \right)$$
$$= -\frac{\partial \bar{P}}{\partial z} + (\nu + \nu_t) \left(\frac{\partial^2 \bar{w}}{\partial x_q \partial x_q} + \frac{\partial^2 \bar{w}}{\partial z^2} \right) + \frac{\partial \nu_t}{\partial x_q} \left(\frac{\partial \bar{w}}{\partial x_q} + \frac{\partial \bar{u}_q}{\partial z} \right) + 2 \frac{\partial \nu_t}{\partial z} \frac{\partial \bar{w}}{\partial z} \tag{14}$$

$$\frac{\partial \bar{u}_q}{\partial x_q} + \frac{\partial \bar{w}}{\partial z} = 0 \tag{15}$$

where (13) and (14) are the in-plane and transverse momentum equations, respectively, and (15) is the continuity equation.

An in-plane semi-discretization is defined for (13)–(14). For this, a SUPG/PSPG finite-element formulation is utilized. This is a stabilized formulation in which two stabilization terms are added to the Galerkin formulation. The PSPG stabilization eliminates the spurious pressure modes that result from the use of incompatible elements, thus allowing equal-order interpolations, which are advantageous in terms of implementation. The form of the stabilization term is

$$S_{\text{pspg}} = \sum_e \int_{\Omega_e} (\tau_{\text{pspg}} \tilde{\nabla} \phi_p) \cdot \mathbf{R}^h \, \mathrm{d}\Omega_e \tag{16}$$

where $\tilde{\nabla} = (\partial/\partial x, \partial/\partial y)$ is the 2-D gradient operator, ϕ_p is the weighting function for the pressure DOFs, and R_q^h is the residual of the in-plane momentum equation. This formulation is seen to be consistent because as the solution converges, $R_q^h \to 0$ and consequently $S_{\text{pspg}} \to 0$. τ_{pspg} in (16) is an intrinsic elemental time scale given as

$$\tau_{\text{pspg}} = \frac{h_e}{2U} \zeta(Re^U) \tag{17}$$

using the formulation of Tezduyar [2]. The characteristic element Reynolds number Re^U is based on a global velocity U and characteristic element length h_e:

$$Re^U = \frac{h_e U}{2\nu} \tag{18}$$

where ν is the kinematic viscosity of the fluid, h_e the element hydraulic diameter,

$$h_e = \left(\frac{4S_T}{\pi} \right)^{1/2} \tag{19}$$

and S_T the element area. The function ζ in (17) is given as

$$\zeta(Re^U) = \begin{cases} Re^U/3, & \text{if } Re^U \leqslant 3 \\ 1, & \text{if } Re^U > 3 \end{cases} \tag{20}$$

The SUPG stabilization eliminates convection-induced oscillations in the velocity field. An additional term

$$S_{\text{supg}} = \sum_e \int_{\Omega_e} (\tau_{\text{supg}} \bar{\mathbf{u}} \cdot \tilde{\nabla} \boldsymbol{\phi}_v) \cdot \mathbf{R}^h \, \mathrm{d}\Omega_e \tag{21}$$

is added to the discretized momentum equation, where $\boldsymbol{\phi}_v$ is the Galerkin vector weighting function for the velocity DOFs and $\mathbf{R}^h$ is again the residual of the in-plane momentum equation. τ_{supg} is another intrinsic elemental time scale. Again using the formulation of Tezduyar [2], τ_{supg} is written

$$\tau_{\text{supg}} = \frac{h}{2\|\mathbf{u}^h\|}\,\zeta(Re_u) \tag{22}$$

where the local element Reynolds number Re_u is based on the local velocity $\mathbf{u}$ as

$$Re_u = \frac{h\|\mathbf{u}^h\|}{2v} \tag{23}$$

and

$$\|\mathbf{u}^h\| = (u^{h2} + v^{h2})^{1/2} \tag{24}$$

The characteristic length h is the element length in the direction of the local flow, or

$$h = 2\sum_{i=1}^{NPE} |\mathbf{s}\cdot\tilde{\nabla}N_i| \tag{25}$$

where NPE is the number of nodes per element, $\mathbf{s}$ is the unit vector in the direction of the local velocity, and N_i is the interpolation function associated with node i.

Performing this in-plane SUPG/PSPG semi-discretization yields

$$\begin{aligned}\sum_e \Bigg[&\int_{\Omega_e} N_i \left(\frac{\partial \bar{u}_p}{\partial t} + \underbrace{\bar{u}_q \frac{\partial \bar{u}_p}{\partial x_q} + \bar{w}\,\frac{\partial \bar{u}_p}{\partial z} + \frac{1}{2}\,\bar{u}_p\left(\frac{\partial \bar{u}_q}{\partial x_q} + \frac{\partial \bar{w}}{\partial z}\right)}_{(h_p)_i} - v\,\frac{\partial^2 \bar{u}_p}{\partial z^2} \right) \mathrm{d}\Omega_e \\ &- \int_{\Omega_e} \frac{\partial N_i}{\partial x_p}\bar{P}\,\mathrm{d}\Omega_e + \int_{\Omega_e} v\,\frac{\partial N_i}{\partial x_q}\,\frac{\partial \bar{u}_p}{\partial x_q}\,\mathrm{d}\Omega_e \\ &+ \underbrace{\int_{\Omega_e} \frac{\partial N_i}{\partial x_q}\,v_t\,\frac{\partial \bar{u}_p}{\partial x_q} - N_i\left(v_t\,\frac{\partial^2 \bar{u}_p}{\partial z^2} + \frac{\partial v_t}{\partial x_q}\left(\frac{\partial \bar{u}_p}{\partial x_q} + \frac{\partial \bar{u}_q}{\partial x_p}\right) + \frac{\partial v_t}{\partial z}\left(\frac{\partial \bar{u}_p}{\partial z} + \frac{\partial \bar{w}}{\partial x_p}\right)\right)\mathrm{d}\Omega_e}_{(b_p)_i} \\ &+ (S_{\text{supg }p})_i \Bigg] = 0\end{aligned} \tag{26}$$

$$\sum_e \left[\int_{\Omega_e} N_i \left(\frac{\partial \bar{w}}{\partial t} + \underbrace{\bar{u}_q \frac{\partial \bar{w}}{\partial x_q} + \bar{w} \frac{\partial \bar{w}}{\partial z} + \frac{1}{2} \bar{w} \left(\frac{\partial \bar{u}_q}{\partial x_q} + \frac{\partial \bar{w}}{\partial z} \right)}_{(h_z)_i} + \frac{\partial \bar{P}}{\partial z} - \nu \frac{\partial^2 \bar{w}}{\partial z^2} \right) \mathrm{d}\Omega_e \right.$$

$$+ \int_{\Omega_e} \nu \frac{\partial N_i}{\partial x_q} \frac{\partial \bar{w}}{\partial x_q} \mathrm{d}\Omega_e$$

$$+ \underbrace{\int_{\Omega_e} \frac{\partial N_i}{\partial x_q} \nu_t \frac{\partial \bar{w}}{\partial x_q} - N_i \left(\nu_t \frac{\partial^2 \bar{w}}{\partial z^2} + \frac{\partial \nu_t}{\partial x_q} \left(\frac{\partial \bar{w}}{\partial x_q} + \frac{\partial \bar{u}_q}{\partial z} \right) + 2 \frac{\partial \nu_t}{\partial z} \frac{\partial \bar{w}}{\partial z} \right) \mathrm{d}\Omega_e}_{(b_z)_i}$$

$$\left. + (S_{\mathrm{supg}\, z})_i \right] = 0 \tag{27}$$

$$\sum_e \left[\int_{\Omega_e} N_i \left(\frac{\partial \bar{u}_q}{\partial x_q} + \frac{\partial \bar{w}}{\partial z} \right) \mathrm{d}\Omega_e + \tau_{\mathrm{pspg}} \int_{\Omega_e} \frac{\partial N_i}{\partial x_q} \left(\frac{\partial \bar{u}_q}{\partial t} + \frac{\partial \bar{P}}{\partial x_q} \right.\right.$$

$$\left.\left. - \nu \left(\frac{\partial^2 \bar{u}_q}{\partial x_p \partial x_p} + \frac{\partial^2 \bar{u}_q}{\partial z^2} \right) \right) \mathrm{d}\Omega_e + (S_{\mathrm{pspg}\, h})_i + (S_{\mathrm{pspg}\, b})_i \right] = 0 \tag{28}$$

where $(S_{\mathrm{supg}\, p})_i$ are the SUPG stabilization terms for the in-plane momentum equations, $(S_{\mathrm{supg}\, z})_i$ the SUPG stabilization terms for the transverse momentum equation, $(S_{\mathrm{pspg}\, h})_i$ the PSPG stabilization terms associated with convection $(h_p)_i$, $(h_z)_i$, and $(S_{\mathrm{pspg}\, b})_i$ the PSPG stabilization terms associated with eddy viscosity $(b_p)_i$, $(b_z)_i$. This formulation requires gradients of the eddy viscosity to be computed. For this, the eddy viscosity is treated as a nodal DOF and derivatives are computed in the usual FE fashion.

The flow is now assumed periodic in the transverse direction and known at discrete points in space. Consequently, the flowfield can be developed as a discrete Fourier sum. That is, any quantity $\theta_n(x, y, t) = \theta(x, y, z_n, t)$ is expressed as

$$\theta_n(x, y, t) = \frac{1}{N} \sum_{k=0}^{N-1} \hat{\theta}_k(x, y, t) \exp\left(\frac{2\pi I k}{N} n \right) \tag{29}$$

where $I \equiv \sqrt{-1}$, N is the number of discrete samples in the set, and L is the transverse dimension of the domain. The equations for the discrete Fourier modes $\hat{\theta}_k$ are obtained by taking the discrete Fourier transform (DFT) of the discrete equations (26)–(28), where the DFT is defined as

$$\hat{\theta}_k(x, y, t) = \sum_{n=0}^{N-1} \theta_n(x, y, t) \exp\left(-\frac{2\pi I n}{N} k \right) \tag{30}$$

Upon execution of the transform, one obtains

$$\sum_e \left[\int_{\Omega_e} N_i \frac{\partial \hat{\tilde{u}}_{pk}}{\partial t} \, d\Omega_e + (\hat{h}_{pk})_i - \int_{\Omega_e} \frac{\partial N_i}{\partial x_q} \hat{\tilde{P}}_k \, d\Omega_e + \int_{\Omega_e} \nu \left(\frac{\partial N_i}{\partial x_q} \frac{\partial \hat{\tilde{u}}_{pk}}{\partial x_q} + N_i \left(\frac{2\pi k}{L} \right)^2 \hat{\tilde{u}}_{pk} \right) d\Omega_e + (\hat{b}_{pk})_i + (\hat{S}_{\text{supg } pk})_i \right] = 0 \tag{31}$$

$$\sum_e \left[\int_{\Omega_e} N_i \frac{\partial \hat{\tilde{w}}_k}{\partial t} \, d\Omega_e + (\hat{h}_{zk})_i + \frac{2\pi I k}{L} \int_{\Omega_e} N_i \hat{\tilde{P}}_k \, d\Omega_e + \int_{\Omega_e} \nu \left(\frac{\partial N_i}{\partial x_q} \frac{\partial \hat{\tilde{w}}_k}{\partial x_q} + N_i \left(\frac{2\pi k}{L} \right)^2 \hat{\tilde{w}}_k \right) d\Omega_e + (\hat{b}_{zk})_i + (\hat{S}_{\text{supg } zk})_i \right] = 0 \tag{32}$$

$$\sum_e \left[\int_{\Omega_e} N_i \frac{\partial \hat{\tilde{u}}_{qk}}{\partial x_q} \, d\Omega_e + \frac{2\pi I k}{L} \int_{\Omega_e} \hat{\tilde{w}}_k \, d\Omega_e + \tau_{\text{pspg}} \int_{\Omega_e} \frac{\partial N_i}{\partial x_q} \left(\frac{\partial \hat{\tilde{u}}_{qk}}{\partial t} + \frac{\partial \hat{\tilde{P}}_k}{\partial x_q} + \nu \left(\frac{2\pi k}{L} \right)^2 \hat{\tilde{u}}_{qk} \right) d\Omega_e + (\hat{S}_{\text{pspg } hk})_i + (\hat{S}_{\text{pspg } bk})_i \right] = 0 \tag{33}$$

The coupling between the Fourier modes in (31)–(33) is contained only in the convective terms. Consequently, explicit temporal treatment of these terms decouples the Fourier modes within each time step, transforming the 3-D problem into a series of independent 2-D problems. All convective ($\hat{h}_p$, $\hat{h}_z$, $\hat{S}_{\text{supg } p}$, $\hat{S}_{\text{supg } z}$, $\hat{S}_{\text{pspg } h}$) and eddy viscosity ($\hat{b}_p, \hat{b}_z$) terms are treated using a second-order explicit Adams-Bashforth method and a pseudospectral approach [3] in which the terms are evaluated in physical space. The $\hat{S}_{\text{pspg } b}$ terms are neglected due to high computational cost and relatively small magnitude (as determined via numerical experiments). The pressure and diffusion terms use an implicit Crank–Nicholson temporal treatment.

Upon performing the integrals in (31)–(33), a linear system of algebraic equations for the nodal DOFs is derived. A node-by-node ordering of the unknowns is used in which all velocity and pressure unknowns at a node are ordered one after the other to form a small 8-component vector (real and imaginary components of u, v, w, and p). Using this ordering, a small 8×8 matrix equation is associated with each node. The SPARSEKIT toolkit [14] is employed to solve the system of equations generated at each time step. A GMRES algorithm with an ILUT preconditioner has been found to provide adequate results in terms of robustness and speed.

4. PARALLEL IMPLEMENTATION

The majority of the computation time is spent setting up and solving the linear systems that arise for each of the Fourier modes at each time step. Consequently, parallelization of this portion of the algorithm is most important and beneficial.

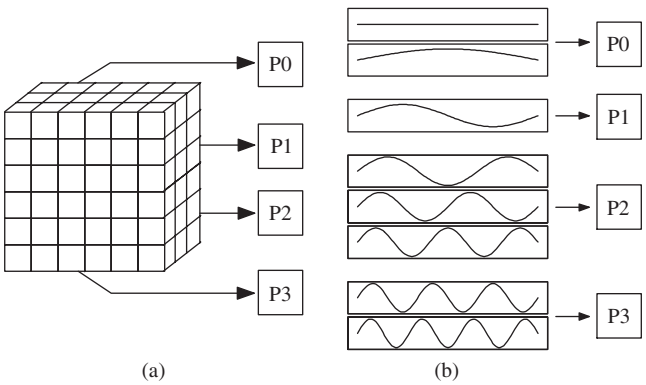

Figure 1. Approaches to partitioning for parallelization: (a) partitioning in physical space and (b) partitioning in Fourier space.

The typical approach taken to parallelize solvers of this type is to partition the computational mesh in physical space, as shown in Figure 1(a). That is, the mesh is divided into *NP* subregions (where *NP* is the number of processors available), and the work associated with each subregion (a submatrix in the overall system matrix) is assigned to a different processor. One drawback to this approach is that the partitioning procedure can be complicated and expensive. Another is that the convergence characteristics and accuracy can change depending upon the partitioning. Yet another is that the submatrices are coupled to one another through the boundaries of the subregions, and information must therefore be passed between processors during the solution of the system.

Because the discretization procedure used in this work produces an independent matrix equation for each Fourier mode rather than a single large coupled system, a novel approach is taken. Rather than partitioning in physical space, the problem is partitioned in Fourier space. As illustrated in Figure 1(b), this means that each Fourier mode is treated as a different thread, or execution path, and can be calculated on a different processor. It is important to understand that rather than using a parallel matrix equation solver as is typically done, NP instances of a serial matrix solver, each solving a different Fourier mode, are called simultaneously.

This approach is free from the drawbacks of the physical space partitioning mentioned above. First, the partitioning process is no longer complicated or expensive. In fact, it is virtually free because it occurs as a natural by-product of the FE/spectral discretization technique. In addition, because the partitions (Fourier modes) are completely decoupled within each time step, accuracy and convergence are not affected by parallelization. Also due to the decoupling of the partitions, there is no need for communication between processors during the system solution.

The parallelization technique is not without its drawbacks, however. As mentioned previously, though the linear system solution takes place in Fourier space, the convective terms are treated with a pseudospectral approach, meaning these terms are evaluated in physical space. Consequently, the flowfield must first be passed through an inverse DFT. This requires that at the end of each time step, all flowfield information from all Fourier modes (all processors) is required in order to calculate the convective terms needed for the following time step. Passing this amount of data between processors on a distributed-memory machine is cost-prohibitive.

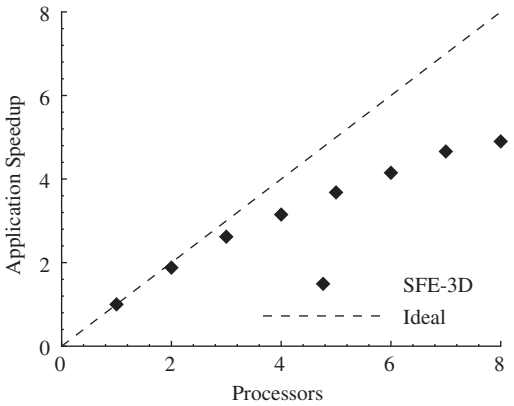

Figure 2. Application speedup as a function of the number of processors.

Another drawback is that load imbalancing is a problem because there are relatively few 'work chunks' (Fourier modes) with possibly varying computational costs. That is, there are only $N/2+1$ linear systems to solve (where N is the number of Fourier modes) and, depending upon the level to which a particular mode is excited, a widely varying amount of time may be required to solve each system.

To address these issues, the parallelization is implemented using OpenMP, an emerging standard for shared-memory parallelism. Using a shared-memory system, all threads can access the same memory locations via a high-speed bus, making the data-passing requirements feasible. An additional advantage to shared-memory machines is that dynamic load scheduling can be used. This approach provides for better load balancing with small numbers of work chunks because threads that finish early 'ask' for more work. Of course, due to the small number of work chunks, the parallelization approach described above is not suitable for massive parallelization—typically using more than $N/4$ processors is not cost-effective.

Figure 2 shows application speed-up (computation time divided by serial computation time) as a function of processors used for a typical circular cylinder test case with approximately 270 000 elements (540 000 nodes)—8500 in-plane elements and 32 Fourier modes. The major reason the actual speed-up falls away from the ideas is the previously-mentioned problem of load imbalancing. Though the dynamic load scheduling helps remedy this, the work chunks are so large and varying that it is common for the solver to be forced to wait while the last work chunk is completed. It should be noted that as more Fourier modes are used, the parallelization becomes more efficient.

5. NUMERICAL EXAMPLE

5.1. Flow configuration

Flow past a circular cylinder in a channel is used to test the above-described algorithm. According to Williamson [5] and Henderson and Barkley [15], at $Re \approx 180$–200, the wake behind a circular cylinder develops streamwise structures of rather large dimension. These

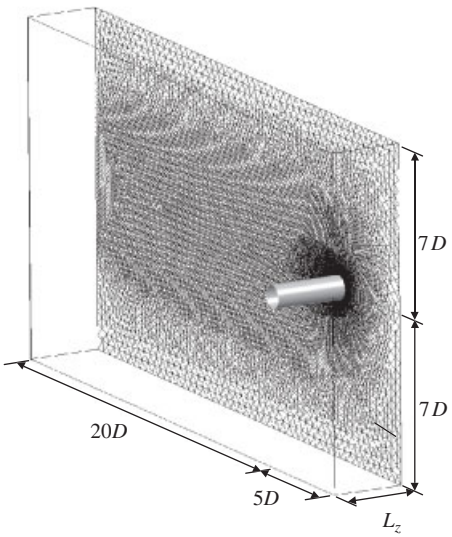

Figure 3. Overview of the computational domain and mesh for the circular cylinder test case.

structures are known as mode-A instabilities and typically have wavelengths on the order of 3–4D, where D is the cylinder diameter. As the Reynolds number is increased to around 260, 3-D structures with wavelengths on the order of 1D, known as mode-B instabilities, become dominant. According to Prasad and Williamson [16], the onset of turbulence occurs at $Re \approx 1200$; it is at this Reynolds number that the shear layers become unstable.

The qualitative correctness of the algorithm developed in this work is verified by its ability to correctly produce mode-A and mode-B instabilities at $Re = 190$ and 300, respectively. In the turbulent regime, $Re = 3900$ is chosen because it has been a popular Reynolds number for experimental and numerical studies of this kind and yet the Reynolds number is low enough such that simulations without wall functions are feasible.

A perspective view of the computational mesh is shown in Figure 3. A Dirichlet velocity inlet condition is applied at the upstream boundary, while a zero-gradient outlet condition exists downstream. Slip-wall conditions are applied at the top and bottom extents of the domain (the blockage effects brought about by these impermeable walls are not accounted for). In the spanwise direction, of course, a periodic condition exists. The effect of spanwise dimension on the flowfield was investigated by Mittal and Balachandar [17]; in accordance with the findings of their study, the spanwise dimension used in this study is $L_z = 2\pi D$ for the laminar cases, and $L_z = \pi D$ for the turbulent case. The reduction in L_z for the turbulent case is a consequence of the decrease in spanwise scales expected in the flowfield.

In the 2-D plane, the standard mesh consists of 23 500 triangle elements with approximately 12 000 nodes. Elements are clustered in the wake region, with characteristic element side lengths of 0.10D in the near wake and 0.19D farther downstream. Outside the wake region the mesh is more coarse, with the characteristic element side length being 0.5D at the upstream and lateral domain extents. Elements are also clustered toward the cylinder in order to better capture the initial development of the turbulent wake. Boundary layer wedge-type elements are used very near the cylinder walls, with the perpendicular dimension of the first element

off the cylinder being $0.0025D$. *A posteriori* analysis shows the first node being located at $y^+ = 1.8$, and around 5 nodes inside the boundary layer at $\theta = 45°$ (with $0°$ being at $y = 0$ on the upstream side of the cylinder) for the $Re = 3900$ case. There exist 110 nodes on the cylinder wall, resulting in an element side length of $0.0275D$. A refined mesh was also generated to verify sufficient spatial resolution. This mesh contains 43 000 in-plane elements with approximately 22 000 nodes. Characteristic element side lengths in the wake region range from $0.071D$ near the cylinder to $0.22D$ near the outlet. The perpendicular dimension of the first wedge-type element off the cylinder is $0.0015D$, and the typical element side length along the cylinder wall is $0.017D$. *A posteriori* analysis shows the first node off the cylinder being located at $y^+ = 1.0$ and about 8 nodes inside the boundary layer at $\theta = 45°$ for the $Re = 3900$ case.

According to the studies by Mansy *et al.* [18] and Williamson *et al.* [19], the spanwise wavelength of the fluid structures near the cylinder scale as

$$\lambda_z/D = \alpha Re^{-1/2} \tag{34}$$

where $\alpha \approx 20$–25. At $Re = 300$ the structures are expected to have wavelengths $\lambda_z/D \approx 1.0$ and at $Re = 3900$, $\lambda_z/D \approx 0.4$. Using a spectral discretization in the transverse direction, at least two points are required per wavelength. Consequently, with $L_z/D = \pi$ a minimum of 16 transverse points are needed to resolve the smallest transverse scales. In this study, 32 points were used in order to ensure sufficient resolution. The overall coarse mesh contains approximately 380 000 nodes, and the fine mesh 700 000 nodes.

The simulations are initialized using potential flow. To decrease computation time, the solution is allowed to develop as a 2-D flow until the Karman vortex street is fully developed. To hasten the development of asymmetric shedding, a time-dependent rotation is applied to the cylinder at the beginning of the simulation for a short time; first in one direction and

Figure 4. (a) Mode-A instabilities at $Re = 195$ and (b) mode-B instabilities at $Re = 300$. Red and blue surfaces mark a positive and negative value of streamwise vorticity, and the yellow and cyan surfaces mark a positive and negative value of transverse vorticity.

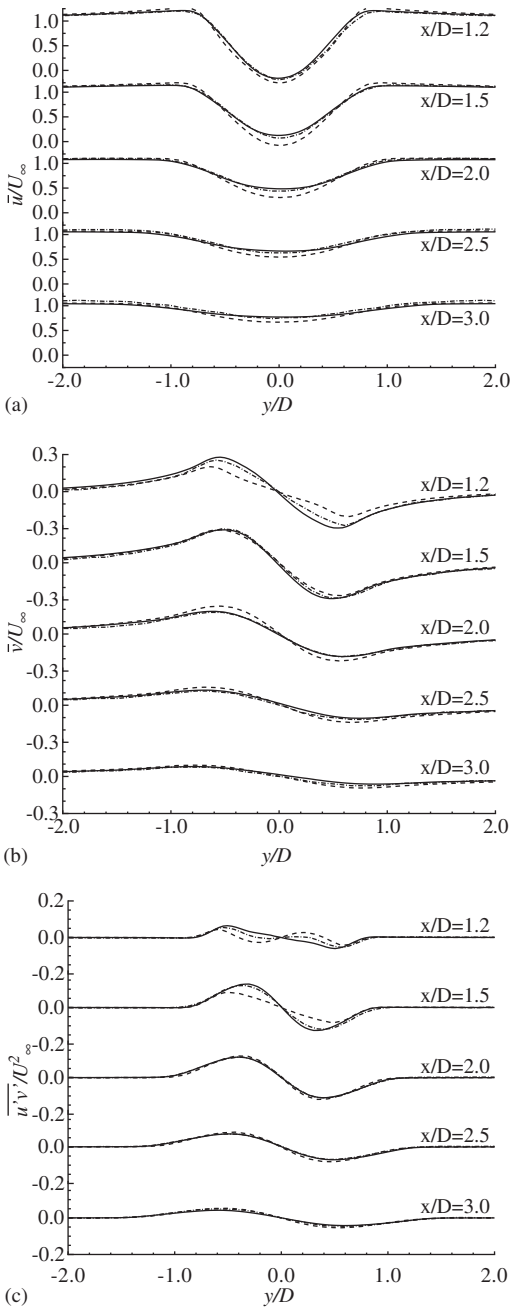

Figure 5. Mean streamwise velocity (a), mean lateral velocity (b), and time-averaged Reynolds shear stress (c) at different streamwise locations in the wake at $Re = 300$. —— fine grid, - - - - - coarse grid, - · - · - B-spline simulations of Kravchenko and Moin [9].

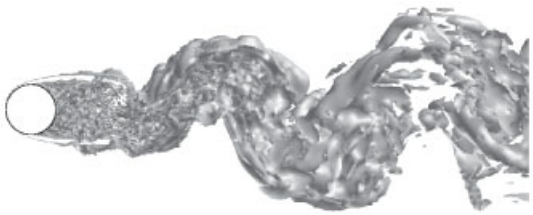

Figure 6. View of instantaneous surfaces of constant vorticity magnitude, $\omega D/U_\infty$, in the region $-0.5D \leqslant x \leqslant 10D$ for flow past a circular cylinder at $Re = 3900$.

Table I. Comparison of flow parameters at $Re = 3900$ with various experiments. C_{D_P} is from Norberg ($Re = 4020$) [22], $\bar{U}_{\min}$ from Lourenco and Shih [9], L_f/D from Cardell [23], θ_{sep} from Son and Hanratty ($Re = 5000$) [24], and St from Ong and Wallace [25]. Unless stated otherwise, the above experimental values were measured at $Re = 3900$.

	$\bar{C}_{D_P}$	$\bar{U}_{\min}$	L_f/D	θ_{sep}	St
Snyder & Degrez	1.09	-0.29	1.30	88.0°	0.2179
Experiment	0.99 ± 0.05	-0.24 ± 0.1	1.4 ± 0.1	$86° \pm 2°$	0.215 ± 0.005

then the opposite. After the 2-D Karman vortex street is sufficiently developed (six shedding cycles, or $T \approx 30D/U_\infty$) a small perturbation is applied at the inlet boundary for a short time ($T \approx D/U_\infty$) to initiate the 3-D features of the flow. The perturbation is of the form

$$u_1' = \varepsilon f(y,z) U_\infty \tag{35}$$

where $\varepsilon = 0.001$, and $f(y,z)$ returns a random number from $(-1,1)$. The simulation is then allowed to advance approximately 10 shedding cycles ($T \approx 50D/U_\infty$) until a statistically steady vortex shedding develops. Finally, the simulation is run an additional six shedding cycles ($T \approx 30D/U_\infty$) to allow calculation of the flow statistics. The time step throughout the simulation is fixed at $\Delta t U_\infty/D = 0.001$. This time step, providing 5000 steps per shedding cycle, is dictated by the stability of the explicit formulation of the convective terms. No turbulent fluctuations are introduced at the inlet, even for the $Re = 3900$ case; because $Re = 3900$ is in the subcritical Reynolds number regime ($Re \lessapprox 100\,000$), the free-stream flow and cylinder boundary layers are laminar—turbulence develops only in the shear layers and wake region.

5.2. Results

Figure 4 shows the qualitatively correct mode-A and mode-B instabilities at $Re = 195$ and 300, respectively. The yellow and cyan surfaces mark constant positive and negative streamwise vorticity, and highlight the alternate vortex shedding. The blue and red surfaces mark constant positive and negative transverse vorticity and show the mode-A structures with characteristic wavelength $\sim 3D$. These results are in excellent agreement with the experiments of Williamson [5] and the computations of Thompson *et al.* [20]. As a quantitative check on the results, the

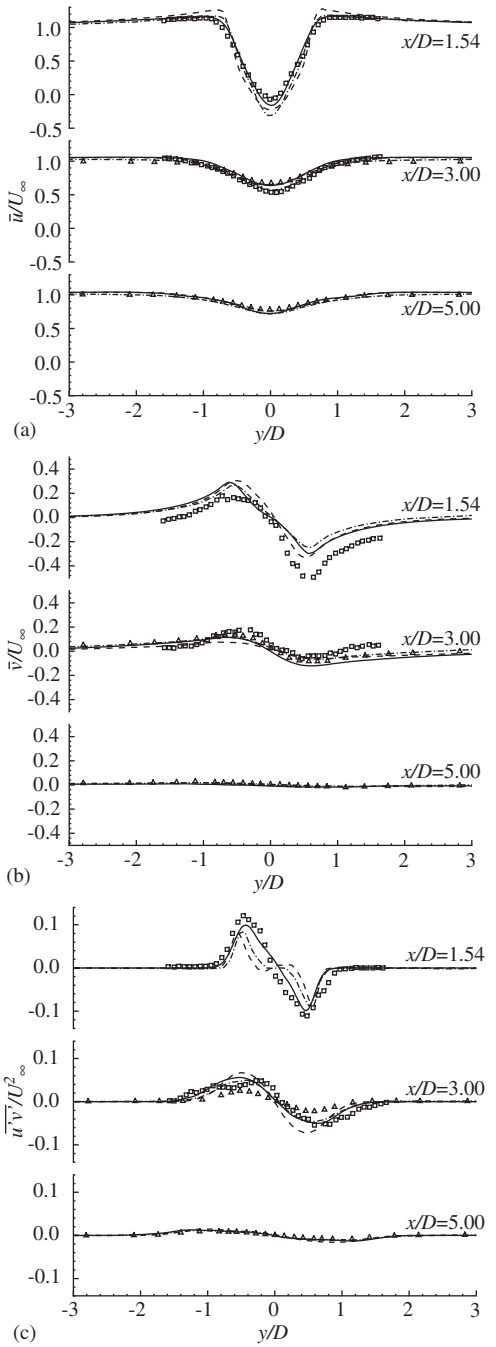

Figure 7. Mean streamwise velocity (a), mean lateral velocity (b), and time-averaged Reynolds shear stress (c) at different streamwise locations in the wake at $Re = 3900$. —— fine grid, - - - - - coarse grid, - · - · - B-spline simulations by Kravchenko and Moin [9], □ PIV measurements of Lourenco and Shih [9], △ hot wire measurements of Ong and Wallace [25].

flow statistics at $Re = 300$ are plotted and compared with the numerical results of Kravchenko and Moin [9] in Figure 5. The statistics are averaged in the transverse direction and over approximately eight shedding cycles and contain results from the standard grid described above and a coarse grid containing approximately 3800 in-plane nodes and 16 Fourier modes. From these plots it is seen that the results of the current algorithm are in good agreement for both the mean velocity components and the time-averaged Reynolds stress.

An instantaneous view of the $Re = 3900$ flowfield is shown in Figure 6 via surfaces of constant vorticity magnitude. The long shear layers attached to the cylinder are seen to roll up into the common Karman vortex street. The length of the recirculation region behind the cylinder is predicted to extend $1.4D$ downstream of the cylinder, which is in agreement with experimental observations at this Reynolds number [21].

Statistical information was gathered over six shedding cycles. Table I shows results for common parameters compared with various experimental values. These results agree very well with the experiments—with the exception of the drag coefficient, they are within the experimental error bounds. More statistical information, in terms of mean velocity components and time-averaged Reynolds stresses is compared with existing values in Figure 7. The numerical results of Kravchenko and Moin [9] were achieved on a mesh with approximately 1.3 million nodes; nearly double the fine mesh used in this work. Yet, it is seen that this algorithm produces results in good agreement with both the numerics and experiments. This highlights the advantage of the SUPG formulation, which provides upwind-accurate results but does not suffer from the overly-diffusive nature of typical upwind schemes.

6. CONCLUDING REMARKS

A finite-element/spectral algorithm for incompressible LES with complex 2-D geometries has been developed in this work. The formulation consists of a SUPG/PSPG finite-element discretization using linear triangle elements in the 2-D plane and a collocated spectral (pseudospectral for the convective and eddy viscosity terms) method in the transverse direction. Temporally, a combination of implicit and explicit second-order schemes are employed. The LES model uses the standard Smagorinski scheme with van Driest damping near solid walls.

Testing of the algorithm was accomplished via application to flow past a circular cylinder at Reynolds numbers up to 3900. Results compared well both qualitatively and quantitatively with published experimental and numerical studies in the laminar and sub-critical turbulent regimes. These results indicate that through further development including wall functions, advanced SGS models, and higher-order in-plane discretizations, this approach can provide high Reynolds number LES solutions for complex geometries on small multi-processor deskside computers.

ACKNOWLEDGEMENTS

D. O. Snyder would like to acknowledge support from a US Air Force Fellowship as well as a NSF Graduate Research Fellowship. The VKI contribution to the research was partially supported by the US Office of Naval Research under Grant N00014-99-1-0834.

REFERENCES

1. Henderson RD. Adaptive spectral element methods for turbulence and transition. In *High-Order Methods for Computational Physics*, Barth TJ, Deconinck H (eds). Springer: Berlin, 1999.
2. Tezduyar TE, Mittal S, Ray SE, Shih R. Incompressible flow computations with stabilized bilinear and linear equal-order interpolation velocity-pressure elements. *Computer Methods in Applied Mechanics and Engineering* 1992; **95**(2):221–242.
3. Orzag SA. Numerical methods for the simulation of turbulence. *Physics of Fluids* 1969; **12**(Supplement II): 250–257.
4. Williamson CHK. Defining a universal and continuous Strouhal-Reynolds number relationship for the laminar vortex shedding of a circular cylinder. *Physics of Fluids* 1988; **31**:2742–2744.
5. Williamson CHK. Three dimensional wake transition. *Journal of Fluid Mechanics* 1996; **328**:345–407.
6. Williamson CHK. Vortex dynamics in the cylinder wake. *Annual Review of Fluid Mechanics* 1996; **28**:477–539.
7. Henderson RD. Details of the drag curve near the onset of vortex shedding. *Physics of Fluids* 1995; **7**: 2102–2104.
8. Mitall R, Balachandar, S. Effect of three-dimensionality on the lift and drag of nominally two-dimensional cylinders. *Physics of Fluids* 1995; **7**:1841–1865.
9. Kravchenko AG, Moin P. B-spline methods and zonal grids for numerical simulations of turbulent flows. *Tech. Rep. TF-73*, Stanford University, Stanford, 1995.
10. Kravchenko AG, Moin P. On the effect of numerical errors in large eddy simulations of turbulent flows. *Journal of Computational Physics* 1997; **131**:310–322.
11. Smagorinski J. General circulation experiments with the primitive equations part I: the basic experiment. *Monthly Weather Review* 1963; **91**:99–164.
12. Fureby C, Tabor G. Mathematical and physical constraints on large-eddy simulations. *Theoretical and Computational Fluid Dynamics* 1997; **9**:85–102.
13. Van Driest ER. On turbulent flow near a wall. *Journal of the Aeronautical Sciences* 1956; **23**:1007–1011.
14. Saad Y. *SPARSEKIT*: *a basic tool kit for sparse matrix computations*. Department of Computer Science and Engineering, University of Minnesota, 1994.
15. Henderson RD, Barkley D. Secondary instability in the wake of a circular cylinder. *Physics of Fluids* 1996; **8**:1683–1685.
16. Prasad A, Williamson CHK. The instability of the shear layer separating from a bluff body. *Journal of Fluid Mechanics* 1997; **333**:375–402.
17. Mitall R, Balachandar S. Effect of three-dimensionality on the lift and drag of nominally two-dimensional cylinders. *Physics of Fluids* 1995; **7**:1841–1865.
18. Mansy H, Yang PM, Williams DR. Quantitative measurements of three-dimensional structures in the wake of a circular cylinder. *Journal of Fluid Mechanics* 1994; **270**:227–296.
19. Williamson CHK, Wu J, Sheridan J. Scaling of streamwise vortices in wakes. *Physics of Fluids* 1995; **7**: 2307–2309.
20. Thompson M, Hourigan K, Sheridan J. Three-dimensional instabilities in the cylinder wake. In *International Colloquium on Jets*, *Wakes*, *and Shear Layers*, Melbourne, Australia, April 18–20, 1994.
21. Anderson EA. Effects of taper and splitter plates on the near wake characteristics of a circular cylinder in uniform and shear flow. *Ph.D. thesis*, University of Notre Dame, 1994.
22. Norberg C. Pressure forces on a circular cylinder in cross flow. In *Proceedings of IUTAM Symposium on Bluff-Body Wakes*, *Dynamics and Instabilities*, Eckelmann H, Graham JMR, Heurre P, Monkewitz PA (eds). Springer: Berlin, 1993.
23. Cardell GS. Flow past a circular cylinder with a permeable splitter plate. *Ph.D. thesis*, California Institute of Technology, 1993.
24. Son J, Hanratty TJ. Velocity gradients at the wall for flow around a cylinder at Reynolds numbers 5×10^3 to 10^5. *Journal of Fluid Mechanics* 1969; **35**:353–368.
25. Ong L, Wallace J. The velocity field of the turbulent very near wake of a circular cylinder. *Experiments in Fluids* 1996; **20**:441–453.

